LAWRENCE
LIVERMORE
NATIONAL
LABORATORY

UCRL-JRNL-236541

Neoclassical Simulation of Tokamak Plasmas using Continuum Gyrokinetc Code TEMPEST

X. Q. Xu

November 14, 2007

Physical Review E

Disclaimer

Neoclassical Simulation of Tokamak Plasmas using Continuum Gyrokinetic Code TEMPEST*

X. Q. Xu*
Lawrence Livermore National Laboratory, Livermore, CA 94550 USA
(Dated: November 8, 2007)

We present gyrokinetic neoclassical simulations of tokamak plasmas with self-consistent electric field for the first time using a fully nonlinear (full-f) continuum code TEMPEST in a circular geometry. A set of gyrokinetic equations are discretized on a five dimensional computational grid in phase space. The present implementation is a Method of Lines approach where the phase-space derivatives are discretized with finite differences and implicit backwards differencing formulas are used to advance the system in time. The fully nonlinear Boltzmann model is used for electrons. The neoclassical electric field is obtained by solving gyrokinetic Poisson equation with self-consistent poloidal variation. With our 4D $(\psi, \theta, \epsilon, \mu)$ version of the TEMPEST code we compute radial particle and heat flux, the Geodesic-Acoustic Mode (GAM), and the development of neoclassical electric field, which we compare with neoclassical theory with a Lorentz collision model. The present work provides a numerical scheme and a new capability for self-consistently studying important aspects of neoclassical transport and rotations in toroidal magnetic fusion devices.

PACS numbers: 52.55.Fa, 52.25.Fi, 52.35.Ra, 52.65.Tt, 52.65.Kj

I. INTRODUCTION

The outstanding scientific problem in the plasma boundary lies in understanding the structure of the edge transport barrier, which forms spontaneously in high-performance (H-mode) discharges in tokamaks. At present, the physics governing the structure of the edge pedestal remains controversial because of the wide range of physical processes, scale lengths, and timescales that come into play. First of all, the fact that the fundamental characteristics of the medium changes from a collisional fluid plasma to a collisionless Vlasov plasma as one moves inward across the pedestal will force us to go beyond the theoretical descriptions of plasma transport presently used in simulations; second, the radial width of the pedestal observed in experiment is comparable to the radial width of individual particle orbits (leading to large distortions of the local distribution function from a Maxwellian); and third the mean-free-path is long compared to the connection length in the hot plasma at the top of the edge pedestal (violating the assumptions underlying a collisional fluid model). In contrast to several gyro-kinetic code developments using particle-in-cell technique [1, 2] in the pedestal region, we adopt the continuum method for our full-F code development for the following reasons: (1).to avoid the intrinsic noise issue associated with finite number of particles. When simulating equilibrium and fluctuations at the same time, the concern over noise is even more serious for fully nonlinear particle code development because the particle noise from equilibrium simulations is on the same order as fluctuation; (2).to utilize existing Fokker-Planck collision packages developed in the community over the years by solving the nonlinear Fokker-Planck collision operator on velocity meshes.

In a magnetized plasma with straight field lines, the particle orbits are circular gyrations and classical diffusion refers to transport of particles due to Coulomb collisions, taking the particle gyro-orbits in the magnetic field into account. In a toroidal magnetic field, a single particle primarily undergoes parallel streaming along the magnetic field line and cross-field drift. The combination of two motions produces various particle orbits when projecting its three-dimensional orbit onto a poloidal cross-sections. The orbits of passing particles are closed curves which do not quite coincide with flux surfaces because of drift motion across the magnetic field. The banana orbits of trapped particles are traced by bounce motion along the field line accompanied by a slow drift motion across the magnetic field with the shape of a banana. Trapped particles are trapped inside a magnetic well, typically outboard of the torus. Neoclassical transport refers to the radial orbital excursions of particles due to Coulomb collisions. The particle radial displacement in one collision time is typically enhanced because the displacement of the gyrocenter from the original magnetic surface is typically larger than the gyroradius. Neoclassical turbulent transport refers to the radial orbital excursions of particles due to small-scale turbulence decorrelation. Therefore the success of neoclassical simulations relies on the accurate numerical description of the passing and trapped particle orbits, Coulomb collisions and turbulence.

In neoclassical plasmas, a radial electric field arises because of different diffusion rates of ions and electrons. This electric field ensures quasi-neutrality and makes the radial fluxes of electrons and ions equal. This flux corresponds to the flux arising from ion-electron collisions. So far, either in particle simulations or continuum simulations, the electrostatic potential is assumed

*URL: http://www.mfescience.org/users/xu/

to be constant on a flux surface. The radial electric field development is evaluated according to the radial Ampere's law averaged over a closed-flux surface $4\pi\langle \mathbf{J}\cdot\nabla\psi\rangle + \partial\langle \mathbf{E}\cdot\nabla\psi\rangle\partial t = 0$ where ψ is the poloidal magnetic flux, $\langle\cdots\rangle$ represents the flux surface average, and $\mathbf{J}$ is the sum of all the current in the plasma, including the classical polarization current, gyroviscosity current, and the ion guiding-center current (the electron current is typically neglected in tokamak geometry because it is smaller than the ion current by a factor of mass ratio m_e/m_i). The steady state neoclassical radial electric field E_ψ on a magnetic surface is obtained from the condition $\langle j_\psi\rangle = 0$. However, this method is incomplete in the sense that the poloidal electric field cannot be solved simultaneously in a consistent way. This is an unsatisfactory situation since the potential varies significantly in the edge plasma around the X-point and in the divertor leg region due to the presheath dynamics. The gyrokinetic Poisson equation is seldom used becasue the small coefficient in front of Poisson operator associated with the gyroradius makes the quation singular when $\rho_i/L_p \ll 1$. Here L_p is a characteristic gradient scale length of plasma profile. For this reason, no single code exists to simulate both neoclassical transport and turbulence. In this paper, we develop a method to efficiently solve the gyrokinetic Poisson equation with double Neumann radial boundary conditions to remove the singularity and to correctly yield the neoclassical radial electric field.

In this paper, we report our present study of neoclassical transport with self-consistent electric field for the first time using a fully nonlinear (full-f) continuum techniques. Because the problem is high dimensional (5D) with complicated particle orbits in phase space, it is not a trivial task to construct the good difference schemes, for example, at the internal boundaries on the $v_\parallel = 0$ surface in phase space, such as the turning points for the trapped particles in real space, and cutting-cells on $v_\parallel = 0$ boundary surface when two sheets of the distribution function (f^+ for $v_\parallel \geq 0$ and f^- for $v_\parallel < 0$) meet. The neoclassical transport involves several types of physics interacting over several scales in time and space: ion orbital dynamics is fast time scale $\sim \omega_b (= v_{Ti}/qR_0), \nu_{ii}$, and small spatial scale length $\rho_{i\theta}$ and the transport is slow time scale $\sim q^2\nu_{ii}\rho_i^2/a^2$ for the evolution of ion temperature, and large spatial scale $\sim a$. The time necessary to establish a rotional steady state is even longer, of order $\epsilon^{-3/2}$ times the neoclassical thermal equilibration times. Here ρ_i is the ion gyro-radius, $\rho_{\theta,i}$ the ion gyro-radius at the poloidal magnetic field, ν_{ii} the ion-ion collision rate, q the safety factor, ϵ the inverse aspect ratio, a the minor radius of torus, and $\rho_i \ll a$. The state of art implicit method has to be used. The paper is organized as follows: gyro-kinetic equations are given in Sec. 2; numerical schemes are presented in Sec. 3; Section 4 describes simulation results; and a summary is given in Sec. 5.

II. GYRO-KINETIC EQUATIONS

Evolution of the plasma species is determined by coupled ion and electron kinetic equations for the time-dependent five-dimensional (5D) distribution functions simplified from H. Qin, et. al. [3] and T. S. Hahm [4]. The gyrocenter distribution function $F_\alpha(\bar{\mathbf{x}}, \bar{\mu}, E_0, t)$ in gyrocenter coordinates: $Z \equiv (\bar{\mathbf{x}}, \bar{\mu}, E_0, t), \bar{\mathbf{x}} = \mathbf{x} - \rho, \rho = \mathbf{b}\times\mathbf{v}/\mathbf{\Omega_{c\alpha}}$ evolves as,

$$\begin{aligned}
\frac{\partial F_\alpha}{\partial t} &+ \bar{\mathbf{v}}_\mathbf{d}\cdot\frac{\partial F_\alpha}{\partial \bar{\mathbf{x}}_\perp} + (\bar{v}_{\parallel\alpha} + \bar{v}_{Banos})\mathbf{b}\cdot\frac{\partial F_\alpha}{\partial \bar{\mathbf{x}}} \qquad (1)\\
&+ \left[q\frac{\partial\langle\Phi_0\rangle}{\partial t} + \bar{\mu}\frac{\partial B}{\partial t} - \frac{B}{B^*_\parallel}\bar{v}_\parallel q\frac{\partial\langle\delta\phi\rangle}{\partial s} - \mathbf{v_{d0}}\cdot(q\bar{\nabla}\langle\delta\phi\rangle)\right]\frac{\partial F_\alpha}{\partial E_0} = C(F_\alpha, F_\alpha),\\
\bar{\mathbf{v}}_\mathbf{d} &= \frac{c\mathbf{b}}{qB^*_\parallel}\times\left(q\bar{\nabla}\langle\Phi\rangle + \bar{\mu}\bar{\nabla}B\right) + \bar{v}_\parallel^2\frac{M_\alpha c}{qB^*_\parallel}(\bar{\nabla}\times\mathbf{b}). \qquad (2)\\
\bar{\mathbf{v}}_\mathbf{d0} &= \frac{c\mathbf{b}}{qB^*_\parallel}\times\left(q\bar{\nabla}\langle\Phi_0\rangle + \bar{\mu}\bar{\nabla}B\right) + \bar{v}_\parallel^2\frac{M_\alpha c}{qB^*_\parallel}(\bar{\nabla}\times\mathbf{b}). \qquad (3)\\
\bar{v}_\parallel &= \pm\sqrt{\frac{2}{M_\alpha}(E_0 - \bar{\mu}B - q\langle\Phi_0\rangle)}, \quad v_{Banos} = \frac{\mu c}{q}(\mathbf{b}\cdot\bar{\nabla}\times\mathbf{b}), \qquad (4)\\
B^*_{\parallel\alpha} &\equiv B\left[1 + \frac{\mathbf{b}}{\Omega_{c\alpha}}\cdot(v_\parallel\bar{\nabla}\times\mathbf{b})\right], \Omega_{c\alpha} = \frac{qB}{M_\alpha c}, \mu = \frac{M_\alpha v_\perp^2}{2B}, \qquad (5)\\
\langle\delta\phi\rangle &= \langle\Phi\rangle - \langle\Phi_0\rangle. \qquad (6)
\end{aligned}$$

Here $Z_\alpha e$, M_α are the electric charge and mass of electrons ($\alpha = e$), ions ($\alpha = i$). $\bar{\mu}$ is the magnetic moment. The left-hand side of Eq. (1) describes the particle motion in the electric field and magnetic field. C_α is the

Coulomb collision operator. The over-bar is used for the gyrocenter variables and $\langle\ \rangle$ denotes the gyroangle averaging. Here a splitting scheme has been used for the electric potential. The field Φ is split into two parts: Φ^0 is the large amplitude and the slow variation part; $\delta\phi$ is the small amplitude and the rapid variation part. E_0 is almost energy.

In the long wavelength limit $k_\perp \rho_\alpha \ll 1$, the self-consistent electric field is typically computed from the gyrokinetic Poisson equation for multiple species

$$\sum_\alpha \frac{\rho_\alpha^2}{2\lambda_{D\alpha}^2}\nabla_\perp\cdot(\ln N_\alpha \nabla_\perp \Phi) + \nabla^2\Phi = -\ 4\pi e\left[\sum_\alpha Z_\alpha N_\alpha(\mathbf{x},t) - n_e(\mathbf{x},t)\right] - \sum_\alpha \frac{\rho_\alpha^2}{2\lambda_{D\alpha}^2}\frac{1}{N_\alpha Z_\alpha e}\nabla_\perp^2 p_{\perp\alpha}. \qquad (7)$$

The n_α and $T_{\perp\alpha}$ are the normalization density and temperature. The ion gyroradius is $\rho_\alpha = v_{T\alpha}/\Omega_\alpha$, the ion thermal velocity $v_{T\alpha} = \sqrt{2T_{\perp\alpha}/M_\alpha}$, the ion gyrofrequency is $\Omega_\alpha = Z_\alpha eB/M_\alpha c$, and the ion Debye length is $\lambda_{D\alpha}^2 = T_{\perp\alpha}/4\pi n_\alpha Z_\alpha^2 e^2$. There are two important distinctions between Eq. (6) and the usual gyrokinetic Poisson equation [4]. Our gyrokinetic Poisson equation is fully nonlinear with the gyrocenter density N_α and perpendicular ion pressure $p_{\perp\alpha}$ calculated from the gyrocenter distribution function $F_\alpha(\bar{\mathbf{x}},\bar{\mu},\bar{E}_0,t)$. The last term of Eq. (7) is the diamagnetic density from the long wavelength expansion of the gyroaveraged gyrocenter density $N_\alpha(\mathbf{x},t)$, i.e., from the pull-back transform. Although the diamagnetic density is small compared to the ion gyrocenter density, it is of the same order as both the polarization density in high-beta plasmas and the difference between ion and electron gyrocenter densities. This equation is an extension of the typical neoclassical electric field model including poloidal variation.

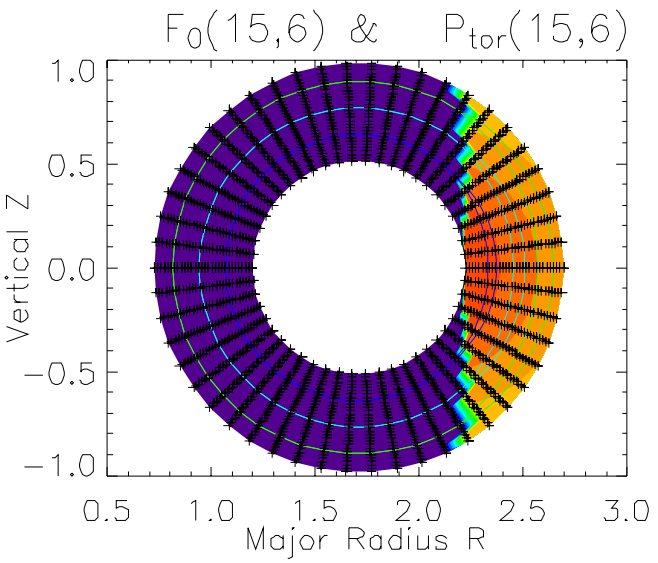

FIG. 1: TEMPEST radial and poloidal meshes in the Ring geometry, indicated by the cross. The contours of distribution function $F_0(\psi,\theta,E_0,\mu)$ with $E_0 = 15$ and $\mu = 6$ in orange represent regions occupied by trapped particles for a given energy E_0 and magnetic moment μ, and is overlaid by trapped particle orbits which is the contour plots of canonical toroidal angular momentum $P_{tor}(\psi,\theta,E_0,\mu) = (q/c)\psi \pm (I/B)M_\alpha v_\parallel$.

III. NUMERICAL SCHEMES

We report on application of TEMPEST, a fully nonlinear (full-f) initial-value gyrokinetic code, to simulate neoclassical transport and the Geodesic-Acoustic Mode (GAM) relaxation in edge plasmas. This 5-dimensional $(\psi,\theta,\zeta,E_0,\mu)$ continuum code represents velocity space via a grid in equilibrium energy (E_0) and magnetic moment (μ) variables, and configuration space via a grid in poloidal magnetic flux (ψ), poloidal angle (θ) and toroidal angle (ζ). The geometry can be a circular annulus or that of a diverted tokamak and so includes boundary conditions for both closed magnetic flux surfaces and open field lines. The same set of gyrokinetic equations are discretized for both geometries. The equations are solved via a Method-of-Lines approach and an implicit backward-differencing scheme using a Newton-Krylov iteration to advance the system in time. The spatial derivatives are discretized with finite differences while a high-order finite volume method is used in velocity space (E_0,μ) for the moment calculations. A fourth-order upwinding algorithm is used for parallel streaming, and a fifth-order WENO scheme is used for particle cross-field drifts. Boundary conditions at conducting material surfaces are implemented on the plasma side of the sheath. The code includes fully nonlinear kinetic or Boltzmann electrons. The gyrokinetic Poisson equation in the long wavelength limit $\rho_i/L_p \ll 1$ is solved self-consistently with the gyrokinetic equations as a differential-algebraic system involving a nonlinear system solve via Newton-Krylov iteration using a multigrid preconditioned conjugate gradient (PCG) solver for the Poisson equation. Here L_p is a characteristic gradient scale length of plasma profile. The code includes a range of options for collisions: simple Krook collision, Lorentz collision and complete linear and nonlinear collision. A nonlinear Fokker-Planck collision operator from STELLA [5] in (v,θ_p) has been streamlined and integrated into the gyrokinetic package using the same implicit Newton-Krylov solver

and interpolating F and $dF/dt|_{coll}$ to/from (ϵ, μ) space, where θ_p is the pitch-angle. The description of the TEMPEST equations, numerical scheme, and verification tests have been given in Ref. [7].

In an axisymmetric configuration, the equilibrium magnetic field is written as $\mathbf{B} = I\nabla\zeta + \nabla\zeta \times \nabla\psi$ where $I = RB_t$. Because the magnetic field is inversely proportional to the major radius ($B \propto 1/R$), for a given energy E_0 and magnetic moment μ, there are inaccessible regions for particles where $v_\parallel^2 = E_0 - \mu B - q\Phi_0 \leq 0$, as indicated on the left side of ring with bluish-violet color in Fig. 1. The crosses are TEMPEST radial and poloidal meshes in the Ring geometry. The contours of distribution function $F_0(\psi, \theta, E_0, \mu)$ in orange represent regions occupied by trapped particles for a given energy E_0 and magnetic moment μ. As the trapped particles move radially outward, the orbit size increases with minor radius, indicated by green curves in the Fig. 1. Therefore there exist internal boundaries for trapped particles in the radial direction. The straightforward upwinding difference yields instabilities near the internal boundary points. Therefore a 5th order Weno scheme [8] is routinely used for particle radial drifts.

There are three constants of motion in an axisymmetric configuration: the total energy $E = M_\alpha v_\parallel^2/2 + \mu B + q\Phi$, the magnetic moment $\mu = M_\alpha v_\perp^2/2B$, and the canonical angular momentum $P_\zeta = (q/c)\psi \pm (I/B)M_\alpha v_\parallel$. The advantage for the choice of (E_0, μ) coordinates is that (E_0, μ) remain constant along particle orbits (in the absence of collisions and turbulence $\delta\phi$), which prevents orbit mixing by numerical differencing, and the dynamics associated with particle orbits can be accurately simulated. The disadvantage is in association of the cut-cells at the bottom of E_0 and top μ-boundary meshes as shown on Fig. 2a), where the boundary $v_\parallel^2 = E_0 - \mu B - q\Phi_0 = 0$ is a straight line cutting through the background grid and separates the physical (above, $v_{||}^2 > 0$) and non-physical (below, $v_{||}^2 < 0$) zone. The dotted line with $E_0 = \mu B(\psi, \theta)$ when $\Phi_0 = 0$ inside physical zone ($v_{||}^2 > 0$) separates the circulating and trapped particles, where the $B(\psi, \theta)$ is the local magnetic field. Obviously, the advantage using (E_0, μ) velocity coordinates is that this physical boundary is NOT a numerical boundary, and therefore there is no additional boundary condition for numerical finite difference across this boundary. The real numerical boundary conditions are as following. (1) There is no flow out of the μ boundary at $\mu = 0$ and $E_0 = 0$; (2) The two sheets of distribution are continuous at $E_0 = E_{0min}$ and $\mu = \mu_{max}$ as shown on Fig. 2b), where $v_{\parallel\alpha} = 0$. Here the two sheets of distribution refer to the distribution with the sign of velocity: f^+ for $v_\parallel \geq 0$ and f^- for $v_\parallel < 0$ for any given energy E_0 and magnetic moment μ. At the top of the μ mesh, the mesh size for a cut cell is $\Delta\mu_{iv,jv} = 2d\mu$, where $d\mu$ is the distance between the $\mu_{max} = (E_0 - q\langle\Phi_0\rangle)/B$ at $v_\parallel = 0$ and the maximum μ-boundary grid point before reaching the μ_{max} at $v_\parallel = 0$ as shown on Fig. 2b), and where the factor of 2 comes

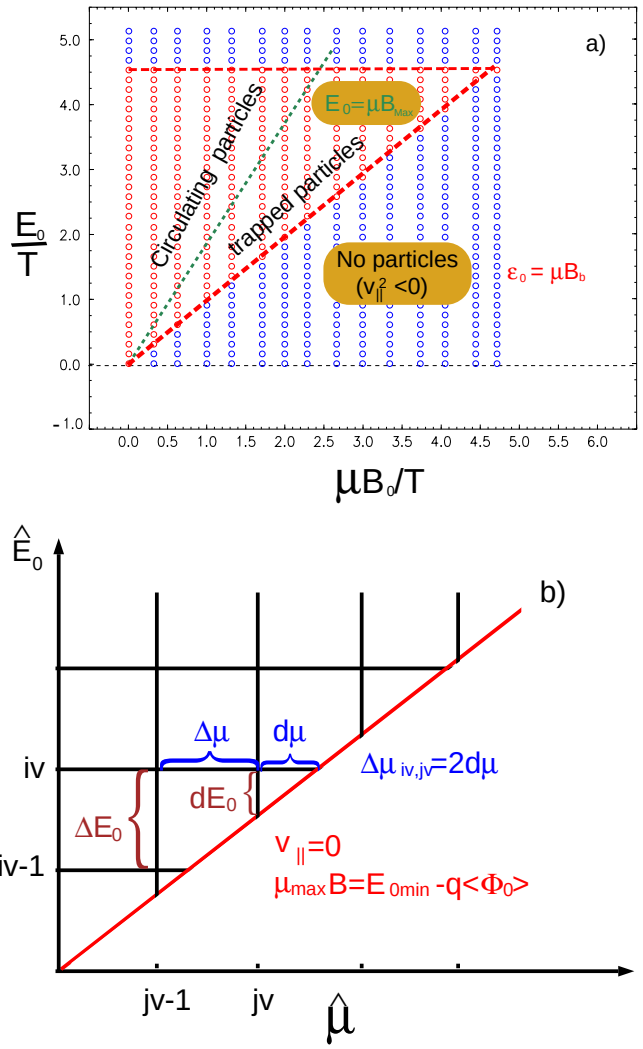

FIG. 2: a) TEMPEST energy E_0 and magnetic moment μ meshes. The boundary $v_\parallel^2 = E_0 - \mu B - q\Phi_0 = 0$ is a straight dashed line cutting through the background grid and separates the physical (above, $v_{||}^2 > 0$) and non-physical (below, $v_{||}^2 < 0$) zone. b) a sketch of cut cells at bottom of the energy E_0 and top of the magnetic moment meshes μ_{max}: $d\mu$ and dE_0.

from the equal distance $d\mu$ to the μ_{max} for the two sheets distribution function. At the bottom of the E_0 mesh, the mesh size for a cut cell is $\Delta E_{0iv,jv} = 2dE_0$, where dE_0 is the distance between the $E_{0min} = (\mu_{Max}B + q\langle\Phi_0\rangle)$ at $v_\parallel = 0$ and the minimum E_0-boundary grid point above the E_{0min} at $v_\parallel = 0$ as shown on Fig. 2b). The cut cells dE_0 and $d\mu$ will have to be merged with its neighboring regular cells if they are too close to the $v_\parallel = 0$ line to avoid arbitrarily small cut-cells, which can lead to small time step by the restrictive Courant-Friedrich-Lewy (CFL) stability constraint. The detailed description of a cell cutting and mergeing scheme is given in Ref. [9]. (3) At top of energy mesh E_{0max} the exponential extrapolation of the distribution F_α in energy is used, assuming $F_\alpha = F_\alpha(E_{0max})exp[-(E_0 - E_{0max})]$ beyond the simula-

tion doman for $E_0 > E_{0max}$.

Radial Robin boundary conditions are used for F_α and potential Φ at the inner core surface $\psi = \psi_c$ and the outer wall surface $\psi = \psi_w$. Robin boundary conditions consist of specification of a linear combination of a field value and its normal derivative at all points of the boundary surface $\psi = \psi_{c,w}$, such as $\alpha_b \Phi^b + \beta_b \partial\Phi^b/\partial\psi$, where $\alpha_b, \beta_b, \Phi^b$ and $\partial\Phi^b/\partial\psi$ being prescribed. This is a generalization of Dirichlet ($\alpha_b = 1$ and $\beta_b = 0$) and Neumann ($\alpha_b = 0$ and $\beta_b = 1$) boundary conditions. Since the gyrokinetic equation has only a first-order radial advection term, only one boundary condition is used and then only where the convection is into the domain. No boundary condition should be imposed for particles convecting out of the domain; therefore an extrapolation is used at that boundary.

For neoclassical transport problems, the scale length of potential L_ϕ is determined by the drift orbit size $\rho_{\theta,i}$ and is typically much larger than the gyro-radius (ρ_i, $L_\phi \sim \rho_{\theta,i} \gg \rho_\alpha$), Here $\rho_{\theta,i}$ is the ion gyro-radius at the poloidal magnetic field. Hence there is a boundary layer in Eq. (7) associated with small parameter $\rho_\alpha/L_\phi \ll 1$. Therefore, the Poisson equation (7) is rarely solved. Instead, a simplified equation for the radial electric field is used [10] with assumption that the electrostatic potential is constant on the flux surface. For edge plasmas, the potential has both radial and poloidal variations due to the endloss in the Scrape-Off-Layer and the assumption is clearly violated. In order to efficiently solve Eq. (7), we develop a scheme here to impose the Neumann boundary conditions $E_\psi = -\partial\phi/\partial\psi = Const.$ at both radial boundary surfaces to eliminate the boundary layer effects. However, when the Neumann boundary condition is used for both radial boundaries $\psi = \psi_c$ and $\psi = \psi_w$, the Poisson problem is ill posed. A technique used is to remove the global net charge from simulation domain to ensure that the Poisson problem is well posed. This constraint is naturally consistent with plasma quasi-neutrality condition. The same technique has been used for doubly periodic boundary conditions. As an illustration, here is a simple example. A 1D Poisson equation on a domain $0 <= x <= a$ with Neumann boundary conditions is $\rho_i^2 \partial^2\phi/\partial x^2 = \sin(2\pi x/a)$ with $\partial\phi/\partial x = 0, (x = 0, x = a)$. Here $\rho_i/a \ll 1$. The solution to the corresponding equation exists only if there is no net source in the domain; that is, by integration, $\partial\phi/\partial x|^{x=a} - \partial\phi/\partial x|^{x=0} = \int_0^a dx \sin(2\pi x/a) = 0$. The solution can be obtained by integration as $\phi(x) = (a/2\pi\rho_i)^2[(2\pi x/a) - sin(2\pi x/a)] + C_0$. There are two noticeable features of the solution: (1) the solution has an undetermined constant C_0. However, the global constant potential has no physical consequence to the gyrokinetic equation. (2) The scale length of potential is determined by the scale length of the source a, not by the small scale length ρ_i at the boundary surfaces. But, when the small scales ($\sim \rho_i$) turbulence along with large scale orbit size $\sim \rho_{\theta,i} \sim 10\rho_i$ co-exists in the source, the same equation can be solved for multiple spatial scale lengths. These are the properties needed for the neoclassical turbulent transport simulations.

IV. SIMULATION RESULTS

In our 4D TEMPEST neoclassical simulations, we consider a simple axisymmetric tokamak with the magnetic field in a circular geometry, given by $\mathbf{B} = B_\zeta \mathbf{e}_\zeta + B_\theta \mathbf{e}_\theta$, where ζ and θ are the toroidal and poloidal angles of a torus, respectively. The poloidal angle θ is chosen such that $\theta = 0$ corresponds to the outboard midplane of the torus. The inverse aspect ratio $\epsilon = r/R_0$ is not assumed to be small, where r is the minor radius. The major radius is given by $R = R_0(1 + \epsilon\cos\theta)$ and toroidal magnetic field $B_\zeta = B_0 R_0/R$. The plasma consists of deuterium ions and electrons. The typical resolution is $n_\psi = 32, n_\theta = 64, n_{E_0} = 25$ and $n_\mu = 50$.

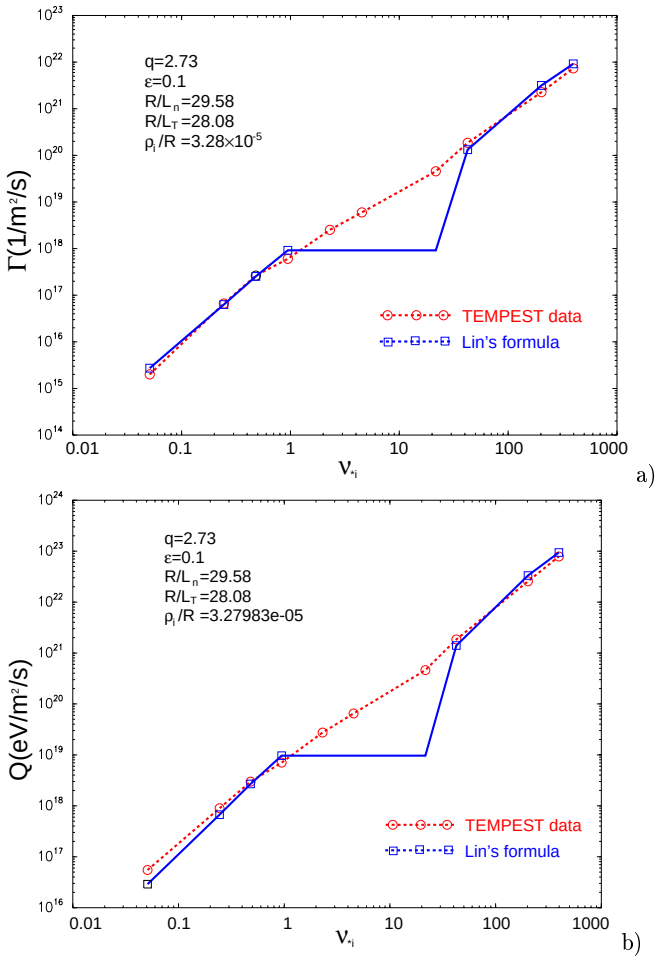

FIG. 3: Radial particle Γ_r (a) and heat flux Q_r (b) vs dimensionless collision frequency ν_{*i} from TEMPEST simulation of neoclassical ion transport with $\phi = 0$. Here a Lorentz collision operator is used. The solid lines are analytical predictions of Lin et al. [11].

A. Neoclassical radial fluxes

Neoclassical transport is the radial orbital excursions of particles driven by collision in a toroidal geometry with an inhomogeneous magnetic field. The simulations presented here are carried out for large aspect ratio circular geometry with magnetic field $B_t = 7.5T, R_0 = 45.6$m, the safety factor $q = \epsilon B_\zeta / B_\theta = 3$ and $\epsilon = 0.1$. The large B_0 and R_0 are used for the global simulations in order to benchmark with analytical theory in the limit $\delta_i / L_p \ll 1$. Here L_p is a characteristic gradient scale length of plasma profile. The ion guiding center density and temperature profiles are initialized as a hyperbolic tangent (tanh) function of radius centered around the middle of simulation domain [such as, $N(\psi) = n_0 + n_m \tanh((\psi - \psi_m)/\Delta_n)$, where $\psi_m = (\psi_0 + \psi_L)/2$ and and $\Delta_n = \delta_n \ln(N(\psi_0)/N(\psi_L))(\psi_L - \psi_0)$]. The boundary ion distribution is a fixed Maxwellian with $N_0 = N(\psi_0), n_L = N(\psi_L) = 0.9N_0, T_{i0} = T_i(\psi_0) = 3keV$, and $T_{iL} = T_i(\psi_L) = 0.9T_{i0}$ during a simulation. The δ_n is a parameter to control the radial scale length. In this simulation $\delta_n = 50.5$. A Lorentz collision model is used. Given boundary conditions and initial profiles, the interior plasmas in the simulations should evolve into a neoclassical steady state.

A series of TEMPEST simulations are conducted to investigate the scaling characteristics of the neoclassical transport as a function of ν_{*i} via a density-scan with $N_0 = (1 \times 10^{12}, 5 \times 10^{12}, 1 \times 10^{13}, 2 \times 10^{13}, 5 \times 10^{13}, 1 \times 10^{14}, 5 \times 10^{14}, 1 \times 10^{15}, 5 \times 10^{15}, 1 \times 10^{16}) cm^{-3}$. Here ν_{*i} is the effective collision frequency, defined by $\nu_{*i} = \epsilon^{-3/2} \nu_{ii} \sqrt{2} q R_0 / v_{Ti}$, ν_{ii} is the ion-ion collision, and the ion thermal velocity is $v_{Ti} = \sqrt{2T_i(\psi_0)/M_i}$. The peaks of both particle and heat fluxes due to the peak radial gradient drives of density and temperature are shown in Fig. 3, along with the analytical predictions of Lin et al [11] using a Lorentz collision operator with a constant frequency. The radial particle and heat flux here and in the rest of paper mean the corresponding flux-surface-averaged fluxes. A time history of the radial heat flux profile in Fig. 4a) for $\nu_{*i} = 4.5$ in plateau regime from TEMPEST shows that the simulation reaches steady state solutions. A good agreement is obtained both in the banana and collisional regimes, where the analytical theories are valid. The flat plateau regime is a theoretical idealization, and the existence has not been observed in the numerical simulations, either Particle-In-Cell code [11] or continuum codes [12, 13].

An interesting property of the neoclassical radial fluxes is checked in the $\nu_{*i} \ll 1$ regime. Since in this regime the collision is negligible small, the particle orbits should be almost closed and therefore there should be almost no net radial fluxes. A time history of the radial heat flux profile is shown in Fig. 4b) for $\nu_{*i} = 0.0006$ with $N_0 = 1 \times 10^{10} cm^{-3}$ in deep banana regime from TEMPEST simulations. The radial heat flux oscillates in time at all radial locations with the same frequency. Fig. 5 shows that after an initial adjustment due to

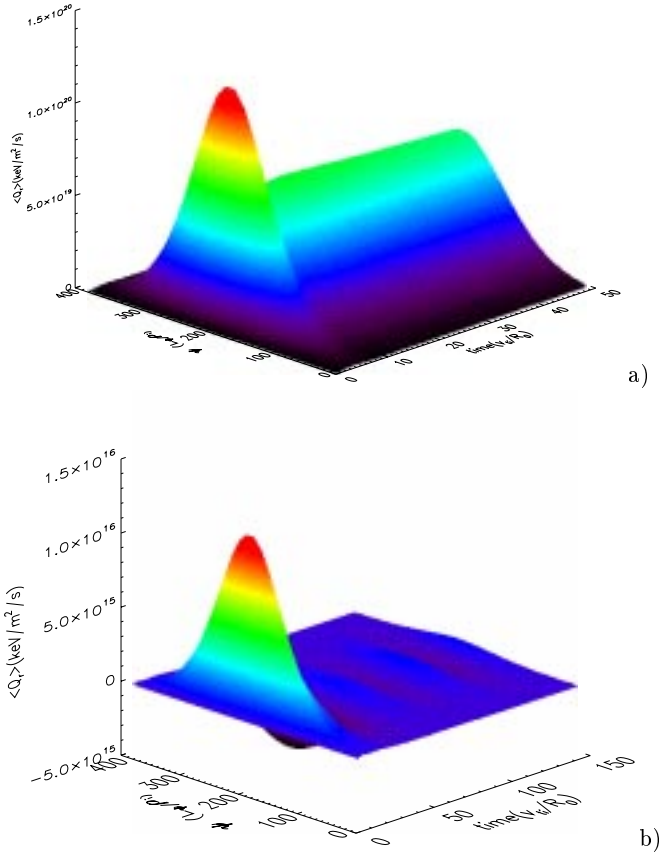

FIG. 4: Radial profile of radial heat flux Q_r for (a) $\nu_{*i} = 4.5$ and (b) $\nu_{*i} = 0.0006$ vs time in the unit of v_{Ti}/R from TEMPEST simulation of neoclassical ion transport with $\phi = 0$. Here a Lorentz collision operator is used.

the arbitrary initial conditions the oscillation frequency is the trapped particle bounce frequency with $\omega_b = \sqrt{\epsilon/2}(v_{Ti}/qR_0), v_{Ti} = \sqrt{2T_i(\psi_0)/M_i}$. The time averaged flux is nearly zero during the late time, which is consistent with the physical expectation.

B. The Geodesic-Acoustic Mode and Neoclassical Relaxation

The Geodesic-Acoustic Mode (GAM) is a poloidally asymmetric mode with a coherent and radially localized poloidal flow oscillation that is dominant in the outer regions of the magnetically confined toroidal plasmas. This mode is characterized by oscillations of the plasma column in the vertical direction with a characteristic frequency $\omega_G \simeq (\sqrt{7}/2) f(q)(v_{Ti}/R_0)$, where $f(q) = \sqrt{1 + 46/49q^2}$, and R_0 is the major radius of a torus. The GAM is a normal mode in a homogeneous plasma, involving particle parallel streaming, cross-field drifts, and acceleration.

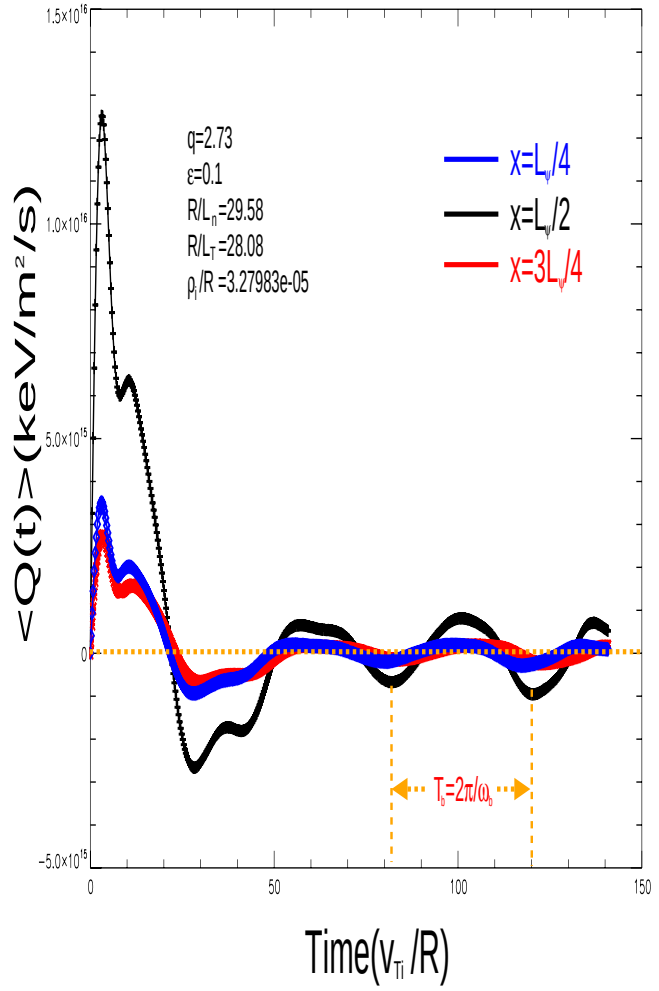

FIG. 5: Radial heat flux Q_r vs time in the unit of v_{Ti}/R from TEMPEST simulation of neoclassical ion transport with $\phi = 0$. Here a Lorentz collision operator is used. Here L_ψ is the radial box size.

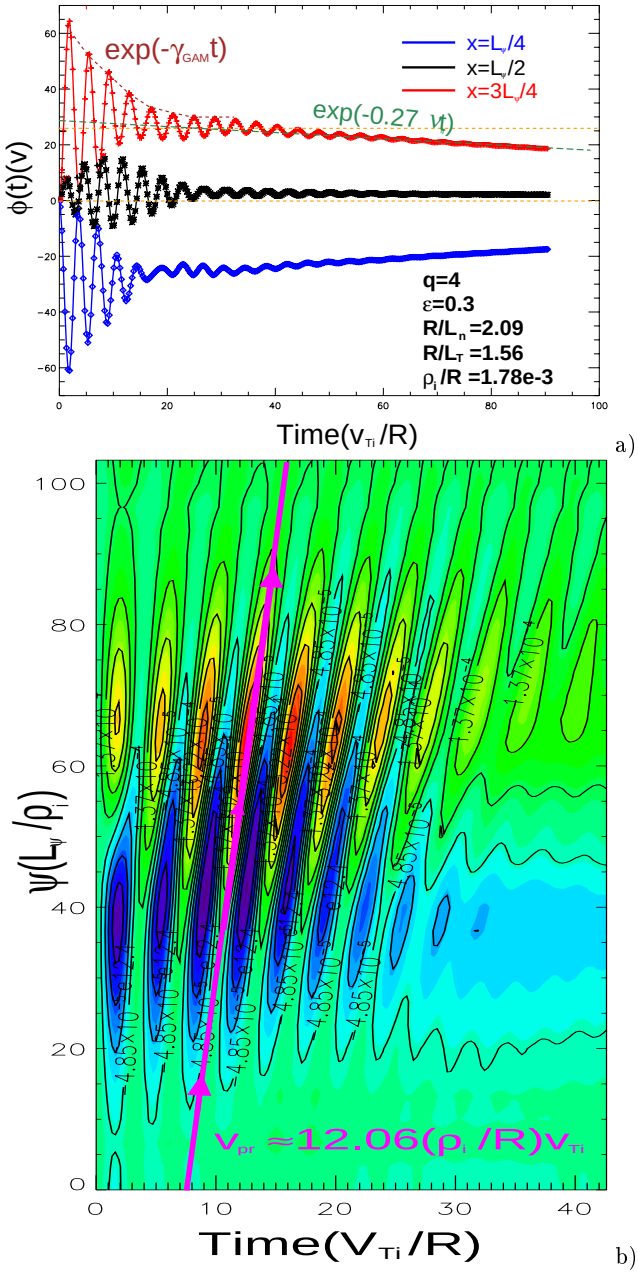

FIG. 6: a) Time evolution of the zonal-GAM potential $\phi(t)$ shows GAM oscillation, collisionless damping, and collisional damping of zonal flow residual for a circular geometry with $q = 4$ and $\epsilon = 0.3$. $n_\psi = 32, n_\theta = 64, n_{E0} = 25$, and $n_\mu = 50$; b) Contour plot of perturbed ion density $\delta n_i/N_{i0} = (N_i - N_{i0})/N_{i0}$ as function of radial position and time for the same parameters. Here L_ψ is the radial box size.

The simulations presented here are carried out for circular geometry with DIII-D edge parameters: magnetic field $B_t = 1.5T, R_0 = 1.71m, q = 4$ and $\epsilon = 0.3$. The ion guiding-center density and temperature profiles are initialized as a hyperbolic tangent (tanh) function of radius centered around the middle of the simulation domain $[N(\psi) = n_0 + n_m \tanh((\psi - \psi_m)/\Delta_n)$, where $\psi_m = (\psi_w - \psi_c)/2$ and $\Delta_n = \delta_n \ln(N_c/N_w)(\psi_w - \psi_c)]$. The δ_n is a parameter to control the radial scale length. In this simulation $\delta_n = 50.5$ and a Lorentz collision model is used. The boundary ion distribution is a fixed Maxwellian with $N_c = N(\psi_c) = 1 \times 10^{19} m^{-3}, N_w = N(\psi_w) = .9N_c, T_{ic} = T_i(\psi_c) = 300eV$, and $T_{iw} = T_i(\psi_w) = 0.9T_{ic}$ during a simulation. The radial boundary condition for the potential is $\partial\phi(\psi_c)/\partial\psi = \partial\phi(\psi_w)\partial\psi = 0$. The electron model is the fully nonlinear Boltzmann model. An initial pulse-like perturbation of the ion density is given with the peak centered around the middle of the pedestal $\delta n_i = \delta N_0(\psi - \psi_m)e^{-(\frac{\psi-\psi_m}{\Delta_{\delta n}})^2}$ where $dN_0 = 0.001$ and $\Delta_{\delta n} = 0.094(\psi_w - \psi_c)$.

A time history of the potential from TEMPEST shows in Fig. 6a) the GAM generated by the initial conditions, damped by the wave-particle resonances and then relaxed to a Rosenbluth-Hinton residual zonal flow. The TEMPEST simulations correctly calculate the GAM frequency ω_{GAM} and the collisionless damping rate γ_{GAM}. The extensive studies of wave-particle resonances and bench-

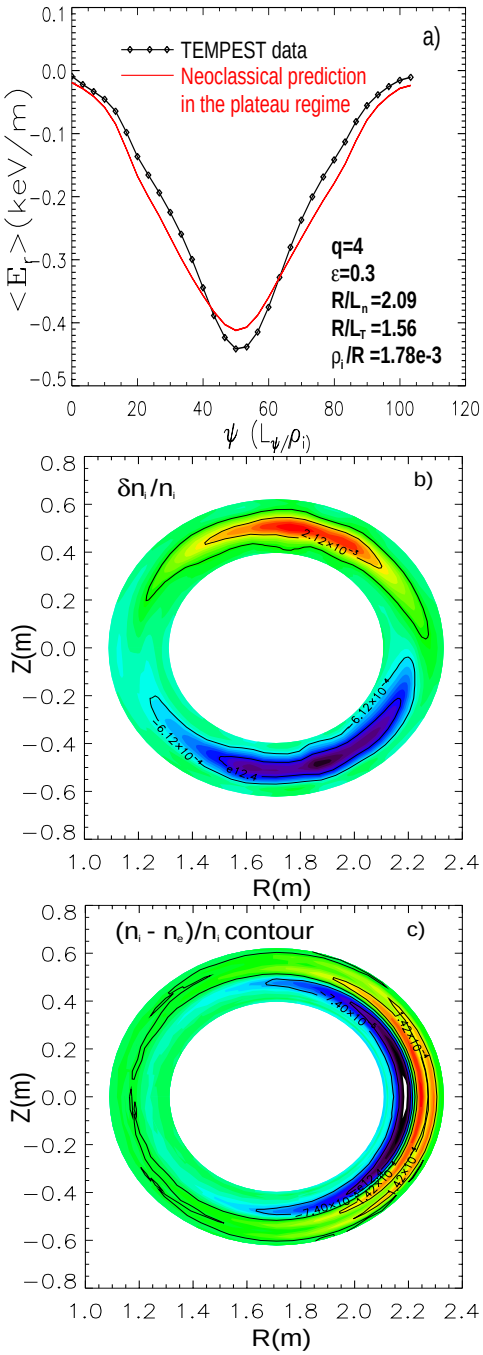

FIG. 7: (a) E_ψ from TEMPEST simulations (black) vs neoclassical prediction in the plateau regime, and contours of (b) the relative perturbed ion density $\delta n_i/N_{i0} = (N_i - N_{i0})/N_{i0}$ and (c) the relative charge density $(n_i - n_e)/n_i$ from TEMPEST simulation of neoclassical ion transport during the GAM oscillations

marking with theory have been demonstrated in Ref. [14]. Fig. 6b) shows contour plot of perturbed ion density as function of the time and radial position. indicating that the GAM exists in the form of a radial eigenmode at a given time. For any given radial location, the GAM oscillates and decays due to the collisionless and collisional damping, as shown on Fig. 6a) of the potential time history. One of the most striking features is that the density perturbation radially propagates outward inside the pedestal where the temperature is inhomogeneous with $v_p \simeq 12.05(\rho_s/R)v_{thi}$ for $q = 4$, which is qualitatively consistent with JFT-2M experimental measurement [15]. The radial propagation velocity v_p is found to be weakly dependent on q, and it increases as q decreases, mostly due to the q-depenence of GAM frequency ω_{GAM} for the fixed plasma profiles.

However, due to the existence of ion-ion collisions, the Rosenbluth-Hinton residual is damped with the damping rate $\propto \nu_{ii}$ as shown on Fig. 6a), and then the potential approaches to neoclassical residual. The collisional damping rate as measured is $\gamma_c \simeq 0.27\nu_{ii}$, which is smaller than the local calculations with $\epsilon \ll 1$ approximation: $\gamma_{HR} = \nu_{ii}/(0.64\sqrt{\epsilon}) \simeq 2.85272\nu_{ii}$ [16] and $\gamma_{XC} = \nu_{ii}/(4\epsilon^{3/2}) \simeq 1.52145\nu_{ii}$ [17]. During the development of the electric field after initial GAM phase, the neoclassical radial electric field from TEMPEST simulations is shown in Fig. 7a), along with the standard neoclassical expression $\langle U_{i\|}\rangle = (cT_i/Z_i eB_p)\,[k(\partial \ln T_i/\partial r) - (\partial \ln P_i/\partial r) - (Z_i e/T_i)(\partial\langle\Phi\rangle/\partial r)]$ with k=-0.5 in the plateau regime [18]. The radial electric field is generated due to the neoclassical polarization. Fig. 7 b) and c) shows the contour of the relative ion density perturbation and the relative charge density from the TEMPEST simulation. Due to the orbital dynamics inside the magnetic well, a particle at the outside midplane streams up and drifts outward from high density to low density on the upper half of the plane, then bounces back from the upper turning point, steams down and drifts inward from low density to high density in the lower half of the plane, bounces back from lower turning point and repeats the process again and agin. The combination of the particle orbits and radial profile of the density yields a poloidal and radial variation of ion density. Because of the large difference in mass ratio between ion and electron, the resulting difference in orbit size creates a neoclassical polarization—a poloidal and radial variation of the charge density, as shown on Fig. 7c).

C. Steady state neoclassical electric field and ambipolarity of neoclassical transport

The simulations presented here are carried out with the same model and parameters as section 4. 2, except in this section $q = 2$ and flat ion temperature profile. Figure 8a) shows the time evolution of electric potential at $x = 0.25L_\psi, x = 0.5L_\psi$ and $x = 0.75L_\psi$. The time unit corresponds to one GAM time (v_{Ti}/R_0). The electrostatic potential relaxes to a steady state, with the GAM in the initial phase damped by Laudau resonance and collision. Fig. 8b) shows the steady-state radial profiles of potential $\phi(\psi)$ (red) and density $\ln(N_i(\psi)/N_i(\psi = 0.5L_\psi))$ (black) from TEMPEST simulations. Here L_ψ is

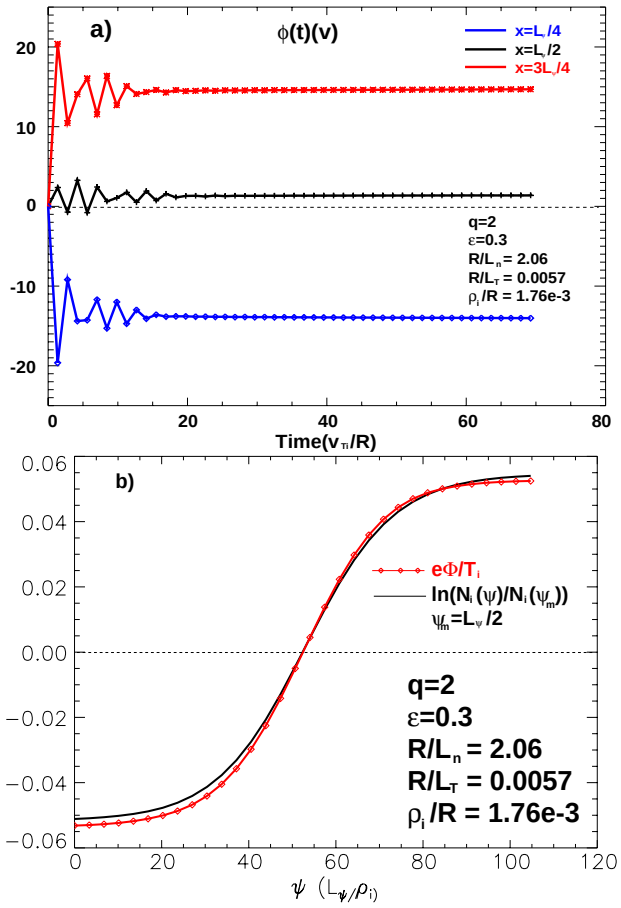

FIG. 8: In circular geometry with DIII-D parameters as in Fig. 7 in the plateau regime, except $q = 2$ and flat ion temperature profile: a) Time evolution of electrostatic potential $\phi(t)$ from TEMPEST simulations at $x = 0.25L_\psi, x = 0.5L_\psi$ and $x = 0.75L_\psi$, b) Steady-state radial profiles of potential $\phi(\psi)$ (red) and density $\ln[N_i(\psi)/N_i(\psi = 0.5L_\psi)]$ (black) from TEMPEST simulations, obeying a Boltzmann relation;

the radial box size. A Boltzmann relation is reached for the steady state potential, as expected from theory for the case of zero temperature gradient [19]. The steady state parallel velocity is very small due to the specified Maxwellian radial boundary condition with zero flow velocity, which accounts for small difference between the two curves in the Fig. 8b). The ambipolarity of neoclassical transport with a self-consistent electric field is numerically demonstrated in Fig. 9a) and compared to the case without E_ψ in Fig. 3a). With no electric field a considerable self-collision driven ion flux is found and violates ambipolarity [20]. By our choice of Boltzmann electrons model, neoclassical electron flux is zero; the quasineutrality constraint forces the net radial ion flux to be zero through the self-consistent radial electric field and its gradient to enforce the orbit squeezing and expassion. The tiny residual flux in Fig. 9a) is possibly due to the non-conserving Lorentz collion model used. Since there is no temperature gradient, the initial GAM exists in the form of a radial eigenmode as a stationary wave without radial propagation as shown on Fig. 9b) and compared to the case with temperature gradient in Fig. 6b). This confirms that the ion temperature inhomogeneity is a key factor for GAM radial propagation.

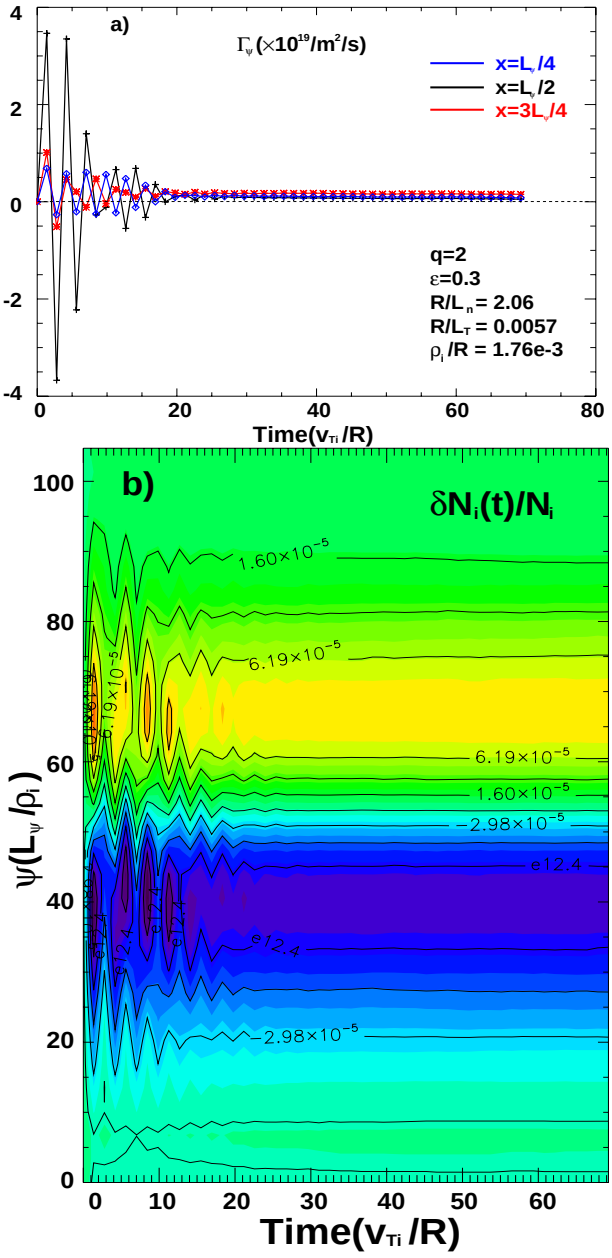

FIG. 9: In circular geometry with DIII-D parameters as in Fig. 7 in the plateau regime, except $q = 2$ and flat ion temperature profile: a) Time evolution of a ion particle flux $\Gamma(t)$ from TEMPEST simulations at $x = 0.25L_\psi, x = 0.5L_\psi$ and $x = 0.75L_\psi$. The local ion flux evolves to a zero steady-state value when the self-consistent electric field is generated. b) Contour plot of perturbed ion density $\delta n_i/N_{i0} = (N_i - N_{i0})/N_{i0}$ as function of radial position and time for the same parameters.

V. DISCUSSIONS AND SUMMARIES

In the development of a 5D gyrokinetic continuum code, we have investigated various choices of velocity coordinates, difference schemes for parallel streaming and radial drift, and verified the numerical simulation results with standard neoclassical theory, using the 4D version of the TEMPEST code with a Lorentz collision. In a very low collision regime, a oscillatory flux in time has been demonstrated, as one might be expected because particles almost stays on the closed orbits.

A numerical technique is presented to efficiently solve the gyrokinetic Poisson equation with double Neumann radial boundary conditions for neoclassical simulations. The simulation results are found to agree very well with the classical theory on the development of neoclassical electric field with a Lorentz collision in banana and plateau regime. In the initial phase of the development of neoclassical electric field, we found that ion temperature inhomogeneity is a key factor for GAM radial propagation. The density and radial electric field perturbation only radially propagates outward inside the pedestal where the temperature is inhomogeneous. Otherwise the GAM exists in the form of a radial eigenmode as a stationary wave without radial propagation. During the development of the electric field afer the initial GAM phase, the neoclassical radial electric field from TEMPEST simulations follows with the standard neoclassical expression for parallel flow in the plateau regime. In the final phase of steady state, the Boltzmann relation is reached between electrostatic potential and ion density for the case of zero temperature gradient, and the quasineutrality constraint forcing the net radial ion flux to be zero is numerically demostrated.

When we tried to use fully nonlinear FP collision package from STELLA, we find that the Fokker-Planck collision calculation is too dissipative due to the coordinate transformation back and forth between energy and magnetic moment space (E_0, μ) with uniform E_0 grid and velocity and pitch angle space (v, θ_p) with non-uniform v grid in Fokker-Planck collision package. The better approach is to develop the nonlinear Fokker-Planck collision operator in term of the fluxes in E_0 and μ space, and interpolate the coefficients of the fluxes from (v, θ_p) to (ϵ, μ) space. The scheme and results will be reported in future publications.

Acknowledgments

This work was performed under the auspices of the U.S. Department of Energy by Lawrence Livermore National Laboratory in part under Contract W-7405-Eng-48 and in part under Contract DE-AC52-07NA27344. We thank Drs. M. R. Dorr, J. A. Hittinger, and P. Colella for math-code infrastructures and software supports, and Drs. E. Belli, J. Candy, B. I. Cohen, R. H. Cohen, R. S. Hazeltine, G. D. Kerbel, W. M. Nevins, S. Krasheninnikov, H. Qin, T. D. Rognlien, P. B. Snyder, M. V. Umansky, W. X. Wang, Y. Xiao, and A. Xiong. for fruitful physics discussions

[1] J. A. Heikkinen, T. P. Kiviniemi, T. Kurki-Suonio, et al., *J. Comput. Phys.* **173**, 527 (2001).
[2] C. S. Chang, S. Ku, and H. Weitzner, *Phys. Plasmas* **11**, 2649 (2004).
[3] H. Qin, R. H. Cohen, W. M. Nevins, and X. Q. Xu, (2006) *Contrib. Plasma Phys.* **46**, 477 (2006); H. Qin, R. H. Cohen, W. M. Nevins, and X. Q. Xu, *Phys. Plasmas* **14**, 056110 (2007).
[4] T. S. Hahm, *Phys. Plasmas* **3**, 4658 (1996).
[5] Kupfer K., R. W. Harvey, O. Sauter, et al., *Phys. Plasmas* **3**, 3644 (1996).
[6] S. D. Byrne and A. C. Hindmarsh, *Int. J. High Perf. Comput. Appl.* **13**, 354 (1999).
[7] X. Q. Xu, Z. Xiong, M. R. Dorr, J. A. Hittinger, *et al.*, Nuclear Fusion **47**, 809-816(2007).
[8] G. S. Jiang and C. W. Shu, *J. Comput. Phys.* **126**, 202 (1996).
[9] Z. Xiong, R. H. Cohen, T. D. Rognlien, and X. Q. Xu, submitted to *J. Comput. Phys.* (2007).
[10] W. X. Wang, N. Nakajima, M. Okamoto and S. Murakami, *Plasma Phys. Control. Fusion* **41**, 1091 (1999).
[11] Z. Lin, W. M. Tang, and W. W. Lee, *Phys. Plasmas* **2**, 2975 (1995).
[12] R. H. Cohen, and X. Q. Xu, *Contrib. Plasma Phys.* (2007).
[13] Belli, E., private communication, 2007.
[14] X. Q. Xu, Z. Xiong, Z. Gao, W. M. Nevins, and G. R. McKee, submitted to *Phys. Rev.Lett.*
[15] T. Ido, Y. Miura, K. Kamiya, *et al*, *Plasma Phys. Control. Fusion* **48**, S41 (2006).
[16] F. L. Hinton and M. N. Rosenbluth, *Plasma Phys. Control. Fusion* **41**, A653 (1999).
[17] Y. Xiao and P. J. Catto, Phys. Plasmas **14**, 055910(2007).
[18] F. L. Hinton and R. D. Hazeltine, *Rev. Mod. Phys.* **48**, 239 (1976).
[19] M. N. Rosenbluth, P. H. Rutherford, J. B. Taylor, E. A. Frieman, and L. M. Kovrizhnikh, in Plasma Physics and Controlled Nuclear Fusion Research, 1970 (International Atomic Energy Agency, Vienna, 1971), Vol. **1**, p. 495.
[20] W. X. Wang and F. L. Hinton, *Phys. Rev.Lett.* **87**, 055002-1 (2001).